

The Whipple Observatory 10 m gamma-ray telescope, 1997–2006

J. Kildea ^{a,*}, R.W. Atkins ^b, H.M. Badran ^c, G. Blaylock ^d, I.H. Bond ^e, S.M. Bradbury ^e, J.H. Buckley ^f, D.A. Carter-Lewis ^g, O. Celik ^h, Y.C.K. Chow ^h, W. Cui ⁱ, P. Cogan ^j, M.K. Daniel ^e, I. de la Calle Perez ^k, C. Dowdall ^j, C. Duke ^l, A.D. Falcone ^m, D.J. Fegan ^j, S.J. Fegan ^h, J.P. Finley ⁱ, L.F. Fortson ⁿ, D. Gall ⁱ, G.H. Gillanders ^o, J. Grube ^e, K.J. Gutierrez ^f, J. Hall ^b, T.A. Hall ^p, J. Holder ^q, D. Horan ^r, S.B. Hughes ^f, M. Jordan ^f, I. Jung ^f, G.E. Kenny ^o, M. Kertzman ^s, J. Knapp ^e, A. Konopelko ⁱ, K. Kosack ^t, H. Krawczynski ^f, F. Krennrich ^g, M.J. Lang ^o, S. LeBohec ^b, J. Lloyd-Evans ^e, J. Millis ⁱ, P. Moriarty ^u, T. Nagai ^g, P.A. Ogden ^e, R.A. Ong ^h, J.S. Perkins ^v, D. Petry ^w, F. Pizlo ⁱ, M. Pohl ^g, J. Quinn ^j, M. Quinn ^u, P.F. Rebillot ^f, H.J. Rose ^e, M. Schroedter ^g, G.H. Sembroski ⁱ, A.W. Smith ^e, A. Syson ^e, J.A. Toner ^o, L. Valcarcel ^a, V.V. Vassiliev ^h, S.P. Wakely ^x, T.C. Weekes ^v, R.J. White ^e

^a Physics Department, McGill University, Montreal, Canada QC H3A 2T8

^b Physics Department, University of Utah, Salt Lake City, UT 84112, USA

^c Department of Physics, Tanta University, Tanta Egleish Street, Tanta, Egypt

^d Department of Physics, University of Massachusetts, Amherst, MA 01003-4525, USA

^e School of Physics and Astronomy, University of Leeds, Leeds LS2 9JT, UK

^f Department of Physics, Washington University, St. Louis, MO 63130, USA

^g Department of Physics and Astronomy, Iowa State University, Ames, IA 50011, USA

^h Department of Physics and Astronomy, University of California, Los Angeles, CA 90095, USA

ⁱ Department of Physics, Purdue University, West Lafayette, IN 47907, USA

^j School of Physics, University College Dublin, Belfield, Dublin 4, Ireland

^k Department of Physics, University of Oxford, Oxford OX1 3RH, UK

^l Department of Physics, Grinnell College, Grinnell, IA 50112-1690, USA

^m Department of Astronomy and Astrophysics, 525 Davey Lab., Penn. State University, University Park, PA 16802, USA

ⁿ Astronomy Department, Adler Planetarium and Astronomy Museum, Chicago, IL 60605, USA

^o Physics Department, National University of Ireland, Galway, Ireland

^p University of Arkansas at Little Rock, Department of Physics and Astronomy, Little Rock, AR 72204, USA

^q Department of Physics and Astronomy, University of Delaware, Sharp Laboratory, Newark, DE 19716, USA

^r Argonne National Laboratory, 9700 S. Cass Avenue, Argonne, IL 60439, USA

^s Department of Physics and Astronomy, DePauw University, Greencastle, IN 46135-0037, USA

^t Max-Planck Institut für Kernphysik (MPIK), P.O. Box 10 39 80, 69117 Heidelberg, Germany

^u Department of Physical and Life Sciences, Galway-Mayo Institute of Technology, Dublin Road, Galway, Ireland

^v Fred Lawrence Whipple Observatory, Harvard-Smithsonian Center for Astrophysics, Amado, AZ 85645, USA

^w N.A.S.A./Goddard Space-Flight Center, Code 661, Greenbelt, MD 20771, USA

^x Enrico Fermi Institute, University of Chicago, Chicago, IL 60637, USA

Received 12 January 2007; received in revised form 2 May 2007; accepted 8 May 2007

Available online 23 May 2007

* Corresponding author. Present address: Fred Lawrence Whipple Observatory, Harvard-Smithsonian Center for Astrophysics, Amado, AZ 85645, USA. Tel.: +1 520 670 5718.

E-mail address: jkildea@gmail.com (J. Kildea).

Abstract

Details are presented of the Whipple Observatory's 10 m atmospheric Cherenkov telescope and camera, as it evolved during the period 1997 until 2006. The design of the telescope and camera's optical and electronic systems is discussed together with a detailed description of the four-stage GRANITE (Gamma-RAY New Imaging TELEscope) upgrade program, undertaken during the same time period. The objective of the upgrade was to improve the telescope's sensitivity for the detection of very-high-energy gamma-rays. Results from the program are provided and are briefly discussed in the context of the design of VERITAS.

© 2007 Elsevier B.V. All rights reserved.

Keywords: Gamma-ray astronomy; Gamma-ray telescope; Atmospheric Cherenkov effect; Imaging atmospheric Cherenkov technique; Whipple collaboration; VERITAS; GRANITE; Imaging atmospheric Cherenkov telescope

1. Introduction

Very High Energy (VHE) gamma-ray astronomy, defined as astronomy in the energy band from 50 GeV to 50 TeV, has developed into an exciting and fruitful field of research [1,2]. The subject has grown through source discoveries made with ever-improving detectors. The primary method for the detection of VHE gamma-rays is the sensitive Imaging Atmospheric Cherenkov (IAC) technique, whereby gamma-ray photons are indirectly detected via the atmospheric Cherenkov light from the air-showers they initiate.

The concept of using the Cherenkov light images of air-showers to enhance the power of the atmospheric Cherenkov technique for gamma-ray astronomy was first pointed out by Jelley and Porter [3]. It was demonstrated by Grindlay [4]. The IAC technique using large reflectors and phototube cameras was proposed by Weekes and Turver [5] and was pioneered by the Whipple Collaboration using the Whipple 10 m telescope [6]. Its first success was the detection of the Crab Nebula (now the standard candle in VHE astronomy) above 0.7 TeV in 1989 [7]. Since then the usefulness of the technique has been further demonstrated by a number of groups worldwide using single IAC telescopes (e.g. CAT [8]) and stereoscopic arrays of two or more IAC telescopes (e.g. HEGRA [9]). At present the field is undergoing rapid development [10], with four major IAC telescope arrays newly built or under construction; VERITAS [11], H.E.S.S. [12], MAGIC [13] and CANGAROO [14].

Central to the IAC technique are two basic requirements: (a) one or more IAC telescopes with sufficient sensitivity to image the Cherenkov light from air-showers and (b) an analysis methodology with the power to separate gamma-ray air-shower images from background cosmic-ray air-shower images. Image-based background rejection is possible due to physical differences in the developments of gamma-ray and hadron showers that are manifested as differences in the focused Cherenkov images they produce. Gamma-ray shower images, due to the smaller transverse momentum and more regular nature of electromagnetic interactions compared with hadronic interactions, are typically narrower and more uniform than their hadronic counterparts. Table 1 lists the important charac-

teristics of the Cherenkov light from air-showers, which IAC telescopes typically measure.

The Whipple 10 m reflector was built in 1968 and was the first large purpose-built atmospheric Cherenkov telescope for gamma-ray astronomy [15]. The telescope has been operated by the Whipple Collaboration as an IAC telescope since 1982. In 1998 the Whipple Collaboration expanded and became the VERITAS Collaboration, which continues to operate the 10 m telescope at this time but which is primarily involved in the construction of VERITAS (the Very Energetic Radiation Imaging Telescope Array System), a third-generation observatory of IAC telescopes [11]. VERITAS will comprise a stereoscopic array of four or more telescopes, each of similar design to the Whipple 10 m. Valuable knowledge and lessons learned during the operation of the Whipple telescope are being incorporated into VERITAS.

Over the course of its lifetime, the Whipple IAC telescope underwent a number of upgrades to improve its flux sensitivity for VHE gamma-rays and to lower its energy threshold. We describe the most recent upgrade, dubbed the GRANITE (Gamma-RAY New Imaging TELEscope) upgrade [16], with a view to putting on record an up-to-date description of the telescope.

The upgrade, begun in 1996 and completed in 1999, was accomplished in four distinct phases: (1) commissioning of a wide field-of-view camera ($\sim 5^\circ$ diameter), (2) installation of a "Pattern Selection Trigger", (3) replacement of the wide field camera with a smaller field-of-view high-resolution camera, and (4) "biased alignment" of the mirror facets to improve the telescope's optics. In this paper we provide a general overview of the Whipple telescope and

Table 1
The characteristics of the Cherenkov light from air-showers that IAC telescopes typically measure

Air-shower property	Value
Cherenkov flash duration	3–4 ns
Cherenkov wavelength range	300–500 nm
Angular size of Cherenkov image	0.5–1.0°
Cherenkov light pool radius	~ 120 m
Cherenkov photon density at sea level	7.4×10^1 photons m^{-2}
Cherenkov photon density at 2.3 km altitude	1.3×10^2 photons m^{-2}

Values are given for typical showers of energy ~ 1 TeV.

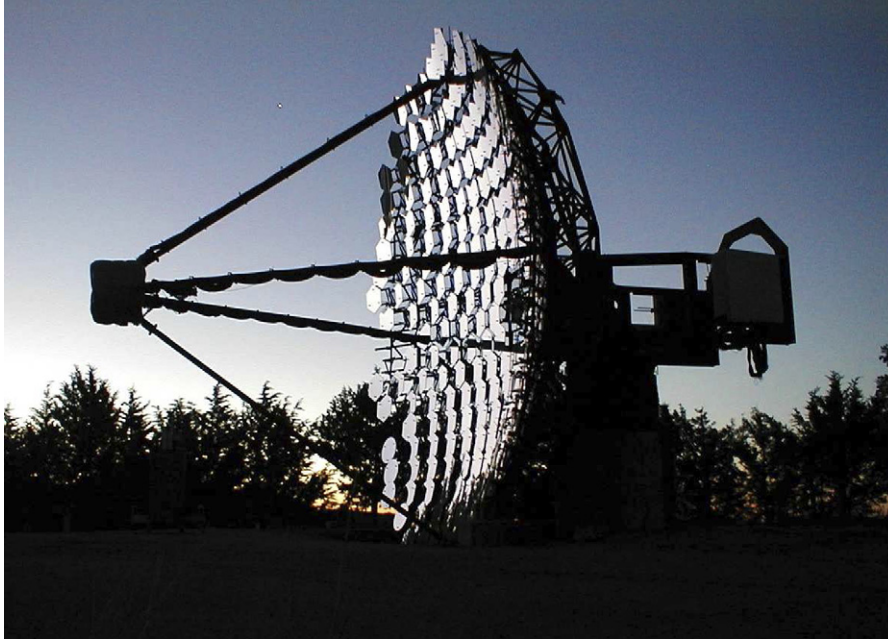


Fig. 1. Photograph of the Whipple 10 m imaging atmospheric Cherenkov telescope on Mount Hopkins, Arizona. The telescope is shown at the stow position.

camera, including some details on calibration measurements and data analysis (Sections 2–4), followed by a detailed description of each stage of the GRANITE upgrade (Section 5), concluding with a short discussion of the improvements realized.

2. The Whipple 10 m telescope

The Whipple 10 m telescope is situated at the Fred Lawrence Whipple Observatory on Mount Hopkins, Arizona (latitude: $31^{\circ}40^m49.7^s$, longitude: $-110^{\circ}52^m45^s.1$, altitude: 2300 m a.s.l.). It has been used for ground-based gamma-ray astronomy since its construction in 1968 and was for many years the most sensitive IAC telescope available; it was used for the detection of the first Galactic [7] and extragalactic [17] sources of VHE gamma-rays.

2.1. Optical and mechanical design

The telescope follows the solar-collector design proposed by Davies and Cotton [18], comprising a spherical tubular steel Optical Support Structure (OSS) of opening diameter 10 m and radius of curvature 7.3 m. The primary dish is composed of 248 spherical front-aluminized and anodized glass mirrors, each 61 cm across, 1 cm thick and hexagonal in shape. Conforming with the Davies–Cotton configuration, each individual mirror has a radius of curvature of 14.6 m, twice that of the OSS. Front aluminization is used for the mirror surface because of its superior reflectivity in the blue and UV range—peak mirror reflectivity is typically around 90% at 310 nm. Anodization of the mirror surface is used to increase its hardness so as to provide protection from the elements,

Table 2
General dimensions and attributes of the Whipple 10 m telescope

Attribute	Value
Opening diameter	10 m
Focal length	7.3 m
F -number	$f/0.73$
Curvature radius of dish	7.3 m
Curvature radius of facet-mirror	14.6 m
Plate-scale in focal plane	12.74 cm/deg
Mount type	Alt/Azimuth
No. of facet-mirrors	248
Reflecting surface area	75 m ²
Tracking resolution	0.01°
Slew speed	1°/s

albeit with some loss in reflectivity (on the order of a few percent). The total mirror surface area of the telescope is approximately 75 m².

The telescope has an altitude-over-azimuth mount supported by a concrete pedestal, with counterweights providing balance. A cylindrical focus box, containing the camera, is held at the focal plane by steel arms. Tracking resolution of the encoders is 0.01°, and the telescope has a slew speed of 1° per second—important for Gamma-Ray Burst follow-up observations. A photograph of the telescope is provided in Fig. 1. Table 2 lists the main mechanical and optical properties.

2.1.1. Mirror alignment

Alignment of the telescope's facet-mirrors is performed when the telescope is positioned close to its stow position, providing for convenient access to the front of the mirrors where the adjustment screws are located. Individual

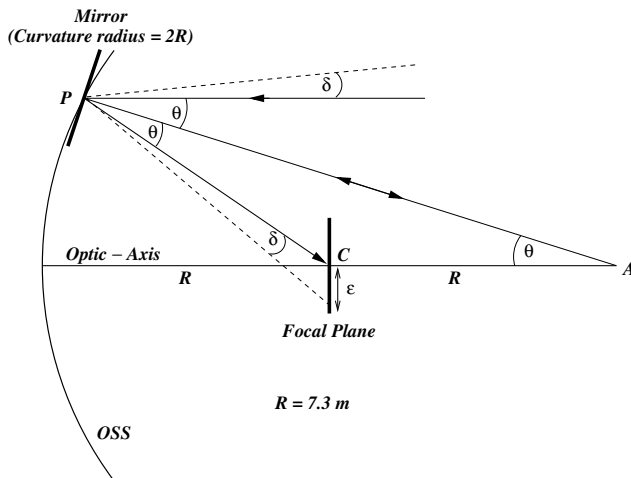


Fig. 2. The Davies–Cotton reflector design. When correctly aligned, the triangle PAC is isosceles and light arriving parallel to the optic-axis is focused onto the center of the focal plane. Rays arriving at an angle δ to the optic-axis are displaced on the focal plane by amount ϵ , in proportion to the plate-scale. Light originating at the alignment point A is retro-reflected along its own path. Figure not to scale.

mirrors are aligned to a point out along the optic-axis at a distance of 14.6 m from the OSS. As shown in Fig. 2, this Davies–Cotton configuration forms a focal surface at the center of curvature of the OSS, 7.3 m away from the mirror surface. According to [19] the Davies–Cotton formation is optimized for no global spherical aberration on the optic-axis and for smaller aberrations off the optic-axis compared to a parabolic design. One disadvantage for gamma-ray air-shower detection, however, is that, unlike a parabolic reflector, the structure is not isochronous. Rays striking mirrors at different distances from the optic-axis have different transit times to the focal plane. For the Whipple telescope the spread of transit times is 6.5 ns.

2.1.2. Mirror reflectivity

For reasons of cost and practicality, the reflecting surface of the Whipple telescope is exposed to the outdoor environment. Deterioration of the unprotected reflective coating and accumulation of air-borne contaminants on the mirrors can affect the optical performance of the telescope. To guard against the build up of contaminants and to maintain the reflectivity of the optical surface, the mirrors are washed monthly and re-aluminized when reflectivity falls below $\sim 75\%$. As part of the GRANITE upgrade project, a study of reflectivity degradation and mirror cleaning methods for the mirrors of the 10 m reflector was undertaken [20]. The study demonstrated that monthly cleaning of the mirrors using only water at high pressure provided the most efficient and inexpensive cleaning method, with little reflectivity degradation (a few percent) over a two year period. Accordingly, the mirrors of the Whipple telescope are washed each month before the beginning of the dark period of observations. Typical mirror reflectivity is in the region of 80–90% at UV wavelengths.

2.2. Focal plane detector

2.2.1. Photomultiplier tube camera

The imaging camera of the Whipple telescope consists of a close-packed array of photomultiplier tubes (PMTs) mounted at the focal plane. PMTs are the most suitable light sensors for IAC telescopes with moderate-sized cameras, due to their fast response (typically on the order of 1–2 ns) and their relatively low noise. Although their quantum efficiency is typically low (15–25%), they are sensitive over a wide wavelength range, from about 200 nm to 600 nm.

Over its 37-year lifetime, the focal plane detector of the Whipple telescope has evolved from a single non-imaging PMT, with a 1° field-of-view, in 1968 to the present 379-pixel high-resolution imaging camera, with each pixel viewing a patch of 0.12° of sky. Schematic layouts of the seven imaging cameras employed on the telescope are shown in Fig. 3, with their corresponding properties listed in Table 3.

2.2.2. High-voltage supply

For the last three camera configurations (Fig. 3e–g), of the GRANITE upgrade cameras, high-voltage to each PMT is supplied by an individual channel of a LeCroy 1458 high-voltage (HV) module, located on the telescope’s counterweights. Voltages are typically in the neighborhood of -900 V. Communication with the HV modules is through custom control software, which sends commands via Ethernet. Although the PMT voltages are set for uniform gain amongst tubes ($\sim 5 \times 10^6$), small differences in gain remain and are corrected for in the offline data analysis. Systematic variations in gain across the camera plane are minimized at the trigger level by appropriate positioning of the PMTs during installation.

2.2.3. Light-concentrators

Light-concentrating cones are employed at the focal plane, in front of the PMTs, to improve the light collection efficiency of the camera. Concentrators help reflect photons which would otherwise be lost in the inter-pixel spacing onto the photosensitive area of each PMT and provide albedo protection against the night-sky-background (NSB) light and the telescope’s surroundings. Typical efficiency improvements provided by light-concentrators are between 30% and 40%. All cameras installed as part of the GRANITE upgrade incorporated light-concentrators in their designs.

2.3. Data acquisition electronics

The Whipple telescope’s data acquisition system is based on individual electronic modules connected to a CAMAC data bus system [21]. The system is housed in an air-conditioned room inside the telescope control building, adjacent to the telescope. The temperature of the electronics room is maintained below 24° Celsius during operation. A schematic overview of the system is provided in Fig. 4.

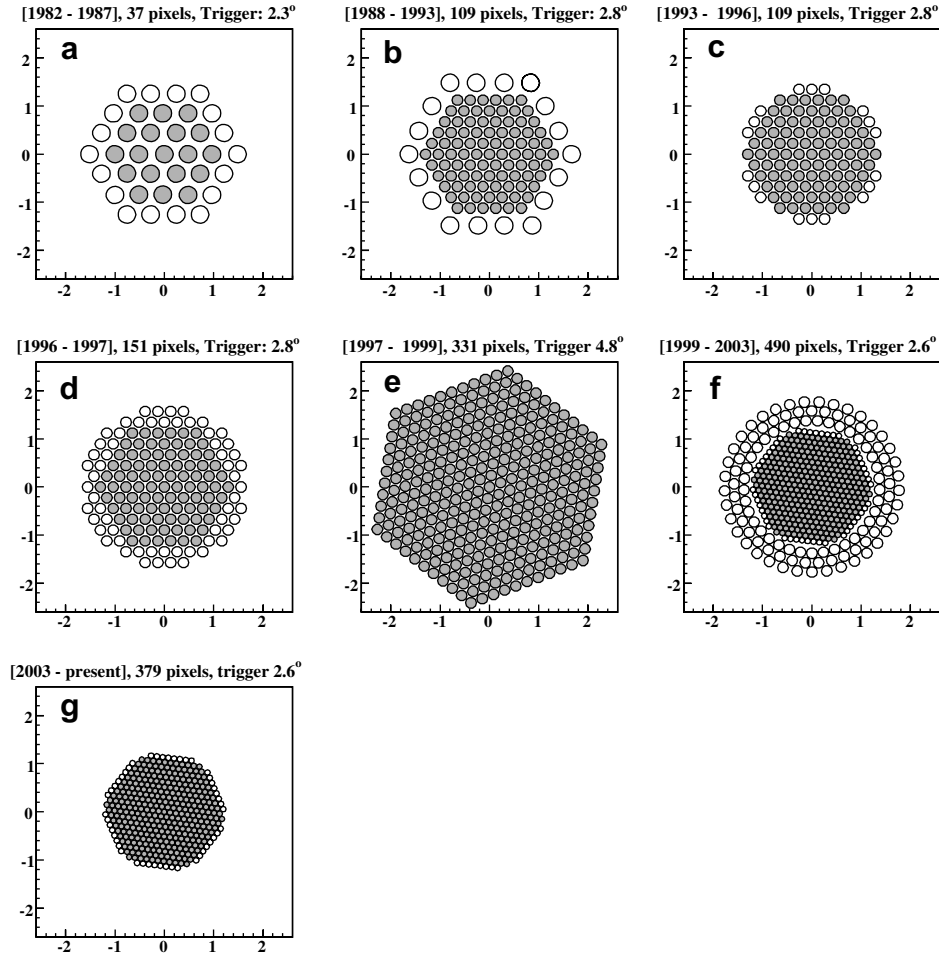


Fig. 3. Schematic diagrams of the PMT positioning for the seven imaging cameras used on the Whipple 10 m telescope over the course of its lifetime. Prior to 1982 a single-pixel non-imaging detector was employed on the telescope. Shaded pixels correspond to those included in the telescope trigger. Axes units are degrees.

2.3.1. Signal amplification and current monitoring

Signals from the PMTs are routed through the hollow steel arms that hold the focus box in position, through the telescope mount and into the telescope control building via 50 m of RG-58 cables, where they are amplified using customized LeCroy 612A amplifiers, each with a gain fac-

tor of 10. Each amplifier has three outputs. The first provides a current monitor with the DC component of the signal. The anode current of each PMT is monitored using custom software and, in the case of high-current (due to bright stars in the field-of-view, background light, etc.), the HV supply to the PMT is turned off by the observer.

Table 3
History of the PMT-camera of the Whipple 10 m IAC telescope

Period	Inner pixels	Outer pixels	Light cones	Pixel FOV (°)	Total FOV (°)	Trigger Coincidence (No. pixels)	Trigger region (No. pixels)	Trigger FOV (°)	PST	CFDs	Trigger Window (ns)	Integration time (ns)	Approx. energy threshold (GeV) ^a
1982–1987	37	0	No	0.52	3.3	2	37	2.3	No	No	15	30	700
1988–1993	91	18	No	0.26/0.52	3.75	2	91	2.8	No	No	15	30	500
1993–1996	109	0	No	0.26	3	2	91	2.8	No	No	15	25	350
1996–1997	151	0	No	0.26	3.5	2	91	2.8	No	No	15	25	350
1997–1998	331	0	No	0.26	4.8	2	331	4.8	No	Yes	10	25	500
1998–1999	331	0	Yes	0.26	4.8	3	331	4.8	Yes	Yes	~5	20	500
1999–2003	379	111	Yes	0.12/0.26	3.8	3	331	2.6	Yes	Yes	~5	20	340
2003–present	379	0	Yes	0.12	2.8	3	331	2.6	Yes	Yes	~5	20	340

Prior to 1982 a single-pixel non-imaging detector was employed on the telescope.

^a Defined as the energy at which the maximum differential gamma-ray rate occurs.

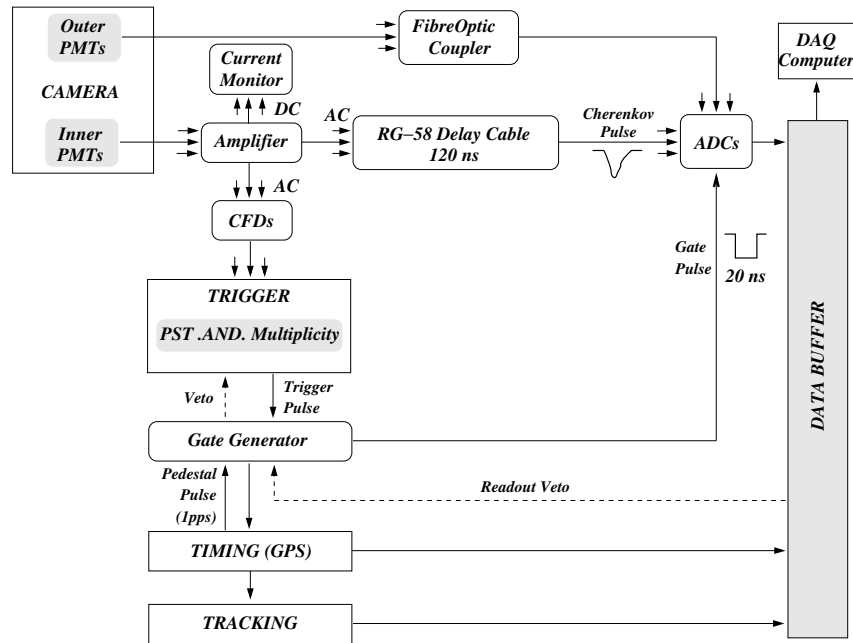


Fig. 4. Overview of the CAMAC-based data acquisition system of the Whipple 10 m telescope. As part of the final stage of the GRANITE upgrade (see text) 111 outer PMTs were incorporated into the camera. The signals from these PMTs were transmitted directly to the ADCs via fiber optic cables. Installation of the fiber optics system was an experiment to test its reliability in an observatory setting. Apart from the specialized electronics required for the outer PMTs, the electronics of the data acquisition system remained unchanged for all stages of the GRANITE upgrade.

The second and third amplifier outputs are AC-coupled, with one connected via delay cable to an analog-to-digital converter (ADC) and the other sent to the trigger electronics (see Fig. 4). For the high-resolution camera, installed as part of the GRANITE upgrade, a system using optical fibers for direct transmission of analog signals from the outer three rings of PMTs to the ADCs was installed and tested (Section 5.3.1).

2.3.2. Trigger electronics

Unlike conventional optical telescopes, which typically integrate the flux of photons from a source on the time scale of seconds, IAC telescopes operate in a triggered mode—PMT signals are only digitized when a shower-like Cherenkov event appears in the camera. On the time scale of the Cherenkov flash from an air-shower (typically ~ 5 ns), detection of the light flash is limited by the fluctuating NSB light, as well as by the timing spread introduced by the telescope and its associated electronics. The trigger systems of IAC telescopes are typically set to reduce the number of false random triggers from the NSB, by requiring that the signals from a minimum number of pixels exceed a preset discriminator threshold (several photoelectrons), and lie within a short coincidence time window (a few nanoseconds). In order to achieve a lower discriminator threshold, accidental NSB triggers and false triggers due to PMT ion-feedback after-pulsing can be further suppressed by a second-level trigger, which uses pixel geometry information to discriminate against random background patterns in favor of compact candidate shower images.

The original trigger of the Whipple telescope comprised a one-level system requiring any 2 out of 91 pixels to cross their fixed-threshold discriminator thresholds, within a coincidence window of 15 ns [6], Table 3. In 1997, LeCroy 3420 Constant Fraction Discriminators (CFDs), one per pixel, were installed during commissioning of the GRANITE wide field-of-view camera (Section 5.1) and the coincidence window was reduced to 10 ns. The use of CFDs allowed for a reduction of the trigger coincidence window as they reduced the pixel-to-pixel time variation that is inherent to fixed-threshold triggering of pulses with differing amplitudes. The CFDs were set to trigger at a level corresponding to 1/3 of the input amplitude. The coincidence window was further reduced to ~ 5 ns in 1998 after installation of the second-level Pattern Selection Trigger, which was typically operated in a three-fold adjacent-pixel coincidence mode (Section 5.2). To maintain a uniform response across the camera under normal operation, the CFD thresholds are set at the same level for all PMTs and are calibrated annually.

2.3.3. Signal recording

Events that trigger the telescope are recorded as ADC digital-count (dc) values per PMT, along with a GPS timestamp and tracking information (azimuth and elevation) from the telescope. AC-coupled signals from the amplifiers are transferred to 10-bit (0–1024 dc) LeCroy 2249 A ADCs via RG-58 delay cable of sufficient length (120 ns) to provide arrival coincident with the trigger gate pulse, which is output by the trigger system in the event of a Cherenkov trigger. A gate pulse of width 20 ns is currently used (see Table 3), over which the PMT signals are integrated by

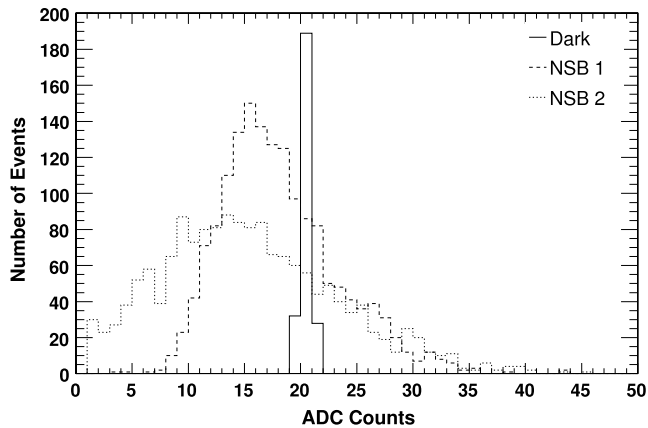


Fig. 5. Pedestal distributions for a sample channel of the high-resolution camera of the Whipple 10 m telescope. Distributions are shown for equal duration measurements made in the dark and for two different levels of night-sky-background noise (NSB 1 = darker, NSB 2 = brighter).

the ADCs. The integration time is longer than the intrinsic Cherenkov flash in order to account for the time spread caused by the anisochronous reflector and signal dispersion in the delay cables. As a consequence, some extraneous light from the NSB is integrated with each Cherenkov pulse. The amount of background light is quantified using non-Cherenkov “pedestal triggers”, injected regularly, and accounted for offline.

The pedestal of an ADC channel is a measure of its mean integrated charge in the absence of a Cherenkov signal. A baseline pedestal amounting to 20 dc is set for each ADC to allow for negative fluctuations in the AC-coupled NSB signal during observations. Artificial telescope triggers, at a rate of 1 Hz, are injected into the data acquisition system in order to measure the resultant pedestal for each ADC (baseline pedestal modulated by NSB fluctuations) during observations. In the absence of NSB light, the width of the pedestal distribution is driven by random noise from the PMTs and the data acquisition electronics. When exposed to the night sky, the distribution is widened depending on the level of the NSB light. The width of the pedestal distribution is used offline to provide an estimate of the level of the NSB over the course of an observation (Section 4.1). Pedestal distributions for a sample channel at different NSB light levels, and in the dark with the PMT covered, are shown in Fig. 5. The linearities of the PMTs used in the GRANITE cameras were measured in the laboratory and they were shown to be linear in the range up to 400 photoelectrons, which was consistent with the manufacturer’s specifications.

2.3.4. Timing electronics

A TrueTime GPS clock (model XL-AK), with absolute accuracy of 250 μ s, provides the main timing information for the Whipple data acquisition system. Through the use of a University of Wisconsin GRS2 memory module and a Canberra 10 MHz oscillator, the GPS time signals are interpolated to 0.1 μ s, providing adequate timing resolu-

tion for pulsar studies. Two 48-bit scalers are used to count pulses from the oscillator and provide the elapsed time and livetime of each event from the start of a data run. The dead time of the data acquisition system, including all contributions from the trigger and readout, is approximately 1% at a typical Cherenkov event rate of \sim 30 Hz.

2.4. Calibration equipment

2.4.1. Nitrogen arc lamp

For PMT-gain calibration purposes an Optitron nitrogen flash lamp is mounted near the center of the OSS, 7.3 m from the PMT-camera. The flash lamp, screened by a diffuser, is used to uniformly illuminate the PMTs with a \sim 750 Hz pulse train of very short duration (several nanoseconds) blue flashes. Nitrogen flash lamp data are used to calibrate the absolute and relative gains of the PMTs (see Section 3).

2.4.2. CCD cameras

A CCD camera, mounted on one of the telescope’s arms and aligned parallel to the optic-axis, is used to monitor qualitatively the sky conditions in the vicinity of the telescope’s field-of-view during data taking. A second CCD camera at the center of the OSS is used to record images of the focal plane during point-spread-function measurements (Section 3.4).

3. Calibration measurements

Accurate calibration of the response of the telescope’s optical and electronic components is essential for efficient online data-taking and correct offline reconstruction of the nature and energy of the imaged air-shower.

3.1. Absolute gain calibration

Calibration of the absolute camera gain is required in order to estimate the flux of Cherenkov photons incident on the telescope for a given air-shower image. The Cherenkov photon flux in turn allows for an estimate of the energy of the instigating gamma-ray. Two methods are used to calibrate the absolute gain: the single-photoelectron and muon-ring methods. Both provide a measurement of the ADC dc value produced by the generation of a single-photoelectron at the photocathode of each PMT, i.e. the dc-per-photoelectron ratio.

Since calibrated gamma-ray and charged particle beams are unavailable at TeV energies, Monte Carlo simulations of gamma-ray and cosmic-ray air-showers, and of the telescope’s response to their Cherenkov emission, are used for the final conversion of the detected Cherenkov photon flux into a gamma-ray energy estimate.

3.1.1. Single-photoelectron calibration

A straightforward method for estimating the camera gain is through its illumination with light of intensity

roughly 1 photoelectron/PMT. For the Whipple 10 m telescope this is achieved by greatly attenuating the light from the nitrogen flash lamp using a thin film of semi-reflective polyester placed in front of the PMTs. By leaving three pixels at the edge of the camera exposed, thus satisfying the requirement for the telescope to auto-trigger, a trigger for each nitrogen flash is initiated, providing readout and integration of all PMT pulses. The resulting ADC count distributions for individual PMTs exhibit two clear peaks; one corresponding to the case of zero photoelectrons (i.e. pedestal) and the other due to single photoelectrons. The ADC count distribution for a sample channel is shown in Fig. 6.

A fit to the ADC count distribution, assuming a Poisson distribution of Gaussian N-photoelectron peaks, allows the mean dc-value of the single-photoelectron peak to be determined. To constrain the fit, the shape of the zero-photoelectron peak is determined independently using a run of pedestal-trigger data, recorded immediately before or after the single-photoelectron data.

3.1.2. Muon ring calibration

While the single-photoelectron measurement provides an accurate measure of the gain of the PMTs and the downstream electronics, it does not provide a measure of the overall telescope gain including the optical system. To obtain such a measurement, the Cherenkov light produced by muons from cosmic-ray-initiated air-showers is used. An individual muon that traverses the atmosphere in the vicinity of an IAC telescope (within a few hundred meters) may produce a sharply defined ring (or arc) image. Since

the angular radius of the ring image is directly proportional to the number of Cherenkov photons emitted by the muon, the recorded light intensity of muon rings can be used as a *de facto* calibration beam, providing the dc-per-photon ratio of the telescope [22]. Atmospheric extinction in the vicinity of the telescope, the muon spectrum and factors that affect the amount of light detected by the PMTs, such as PMT quantum efficiency, mirror reflectivity and lightcone efficiencies, are accounted for using muon and detector simulations. With all sources of light loss accounted for, an estimate of the telescope's dc-per-photoelectron ratio is calculable using muon-ring images, selected from the data by a ring-fitting selection algorithm [23].

3.2. Air-shower and telescope simulations

Monte Carlo simulations of extensive air-showers, together with detailed reflector and electronic throughput simulations, are used to model the response of the Whipple telescope. The KASCADE air-shower simulation package [24] is used to provide air-shower simulations. Cherenkov light emission, photon ray-tracing through the telescope optics, and electronic throughput simulations are undertaken using custom-written algorithms [25,26]. The simulation chain is able to reproduce important diagnostic quantities seen in the real data, including the cosmic-ray trigger rate.

3.3. Relative gain calibration

Relative PMT gains are measured at the beginning of each observing night by uniformly illuminating the PMT-camera using the Optitron nitrogen flash lamp. The relative gain factors are obtained by comparing the mean signals seen by each PMT. Prior to image analysis the recorded pixel signals are scaled by their relative gains to account for efficiency differences amongst the PMTs, see Section 4.1.

3.4. Point spread function

The Point Spread Function (PSF) of the telescope is measured by directly imaging stars on the focal plane using a CCD camera. Both on-axis and off-axis measurements are undertaken. The size of the PSF depends on the quality of the mirror alignment. Ideally it should have a FWHM less than the angular size of the individual pixels in the camera (i.e. 0.12° or less). During observations, the PSF degrades due to a combination of two factors: gross deformation of the OSS and individual mirror motion. These effects can be lessened by aligning the mirrors so that they fall into correct alignment at observing elevations [23] and by periodic realignments. Following installation of the high-resolution camera as part of the GRANITE upgrade a biased alignment was undertaken, providing for a PSF of $\sim 0.12^\circ$ at observing elevations (Section 5.4).

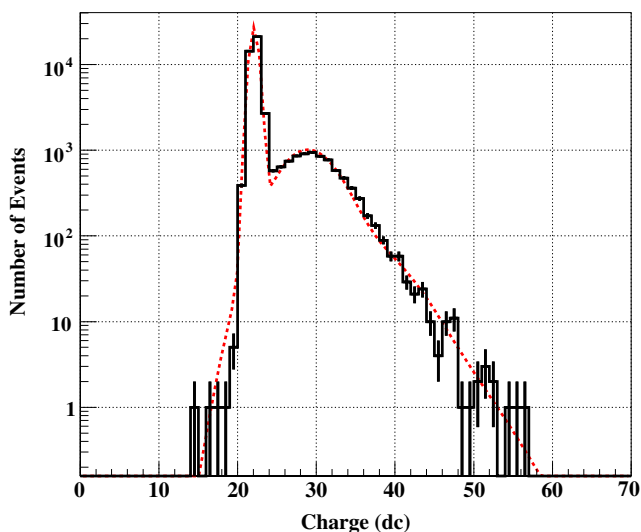


Fig. 6. ADC count distribution for a sample channel for a single-photoelectron run, showing the pedestal (zero-photoelectron) and one-photoelectron distributions. The dashed red line is a fit to the distribution for a Poisson distribution of four Gaussian photoelectron peaks. These data were obtained by attenuating the signal from the Nitrogen flash lamp using a thin sheet of semi-reflective polyester placed in front of the PMT-camera, such that the mean signal recorded by each PMT contained on average one photoelectron or less.

3.5. Telescope pointing accuracy

The variance of a PMT's pedestal distribution provides a measure of the NSB in its field-of-view. As such, the pedestal variance distribution across the camera may be used to characterize the telescope's pointing accuracy; the centroid of the camera's pedestal variance distribution, recorded while briefly tracking a star, provides the tracking offset at the star's azimuth and elevation. This methodology was employed to provide the offline tracking corrections used in the reported Whipple 10 m detection of a gamma-ray excess from the direction of the Galactic Center [27].

4. Observations and data analysis

Gamma-ray source observations are undertaken with the Whipple 10 m telescope on clear, moonless nights. Observations are typically conducted in either "ON/OFF" or "Tracking" mode [28,29]. In ON/OFF mode an observation of a source, typically 28 min duration, is followed by an observation of a control region of sky, across the same azimuth and elevation range as traversed by the source. A gamma-ray signal from the source manifests itself as an excess of ON over OFF events after data analysis. In Tracking mode, on-source only observations are conducted; an estimate of the cosmic-ray background is obtained by examining images in the field-of-view that are not consistent with gamma-ray showers originating at the expected source location.

Analysis of air-shower images recorded by the Whipple telescope is a two-step process: (i) conditioning of each image to remove hardware and NSB effects, and (ii) moment-fitting and selection of gamma-ray images.

4.1. Image conditioning

Image conditioning essentially involves pedestal subtraction, suppression of noise-dominated pixels and camera flat-fielding through application of the relative gains calculated from nitrogen flash lamp data [30]. Any differences that might exist between the levels of NSB light in ON and OFF data, as measured using ADC pedestal variances, are also accounted for at this stage by adding software noise to the data so as to balance the pedestal variances [31].

4.2. Moment fitting and event selection

Conditioned data are analyzed for a gamma-ray signal using a second-moment-fitting parameterization technique that characterizes the angular shape and orientation of each image in the telescope's field-of-view [32,30]. Gamma-ray selection criteria that exploit measurable differences in the image morphologies of gamma-rays and background cosmic-rays are used to extract gamma-ray events and suppress the cosmic-ray background. Selection

criteria are typically motivated by simulations but optimized on real Crab Nebula data. More detailed descriptions of the moment-fitting and event selection procedures are provided by Reynolds et al. [33], Fegan [30,34] and Lessard et al. [35].

5. GRANITE upgrades

5.1. Upgrade 1: Wide field-of-view camera

The first stage of the GRANITE upgrade involved installation of a 331-pixel wide field-of-view camera, during the summer of 1997. The total field-of-view of the camera was 4.8° ; the largest field-of-view of any camera used on the Whipple telescope. A schematic layout of the camera's hexagonally symmetric PMT array is provided in Fig. 3e.

The 331 PMTs used were 28 mm Hamamatsu R1398 UV-glass tubes, each viewing a 0.26° diameter patch of sky. The quantum efficiency of a sample tube from this camera, over the wavelength range 190–550 nm, is presented in Fig. 7. The camera was operated with an overall trigger threshold of ~ 65 photoelectrons, and a 2-fold coincidence trigger condition. Light-concentrating cones were installed in front of the PMTs at the focal plane to reduce the dead space between pixels; dead space for this camera before lightcones was $\sim 48\%$. The lightcones used were intersecting straight cones, fabricated from an aluminum plate with reflective surfaces made from aluminized mylar. Addition of the lightcones increased the light collection efficiency of the instrument by $\sim 30\%$.

To assess the gain in sensitive field-of-view yielded by installation of this camera, a series of off-axis Crab Nebula observations were undertaken. These data are compared in Fig. 8 to similar observations made with the previous (Fig. 3d) and subsequent (Fig. 3g) smaller field-of-view cameras. In each case the Crab Nebula was positioned on-axis and then at two positions off-axis, so as to cover the complete field-of-view of each camera. Inspection of

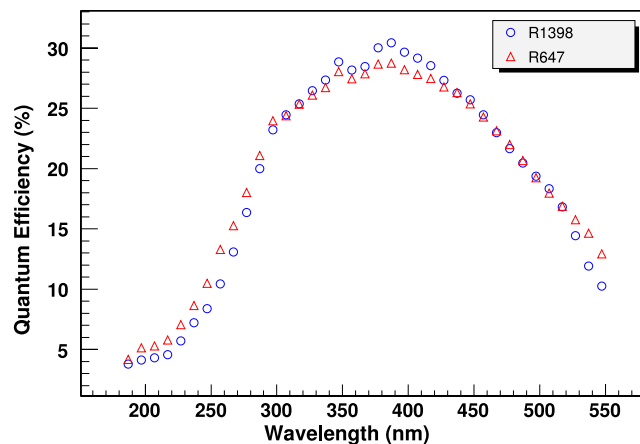


Fig. 7. On-axis quantum efficiency as a function of wavelength for a sample PMT from each of the wide field-of-view (R1398) and high-resolution cameras (R647).

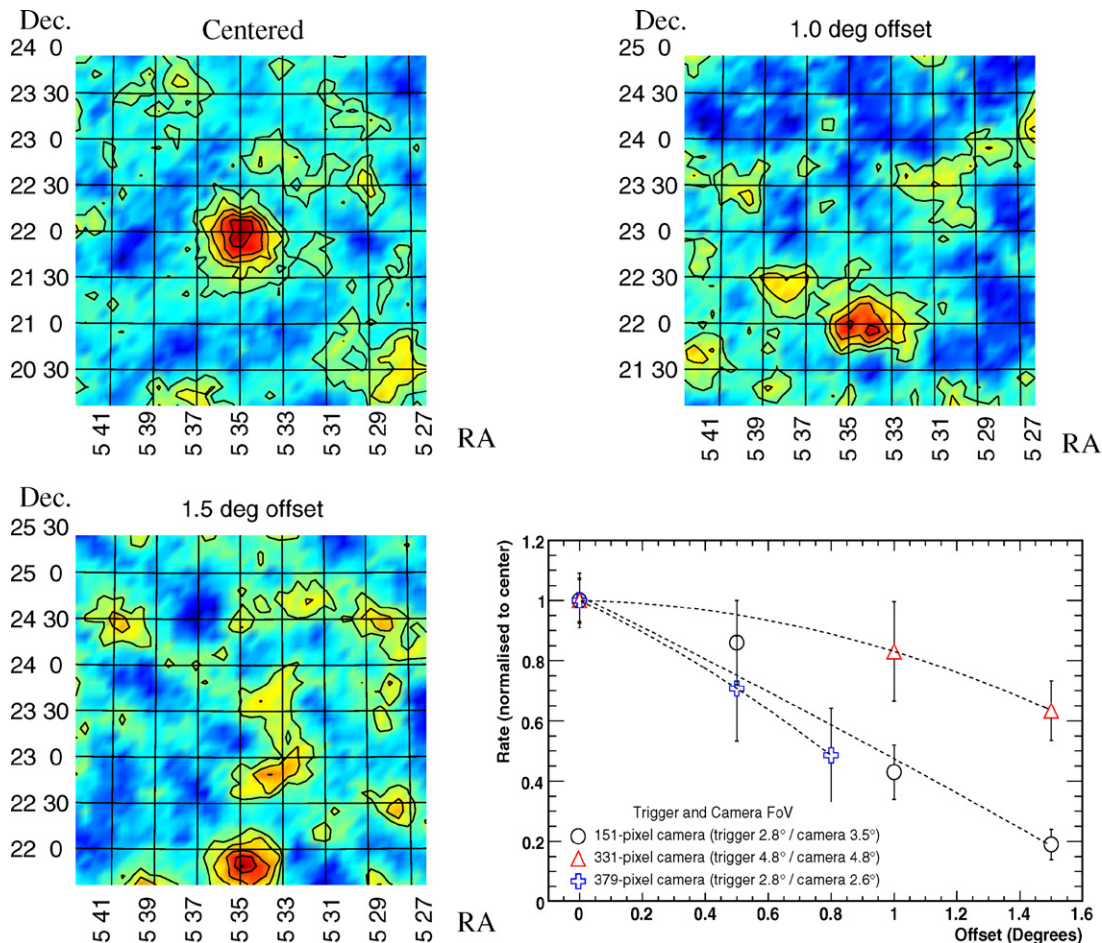


Fig. 8. Effect of field-of-view (FoV) on offset observations: Offset Crab Nebula observations carried out with the 331-pixel wide FoV camera with the source positioned on-axis (upper left), offset by 1.0° in declination (upper right), and offset by 1.5° in declination (lower left). Contours represent gamma-ray significance levels of 1σ . The diagram in the lower right shows the relative Crab Nebula gamma-ray rate as a function of off-axis position, for the 331-pixel wide field-of-view camera, the subsequent 379-pixel high-resolution camera and the previous 151-pixel camera used on the Whipple telescope.

Fig. 8 shows that the wide field-of-view instrument provided a significant increase in sensitive field-of-view compared to the other two cameras. Although only employed on the Whipple telescope for approximately one year, the wide field-of-view camera was used to observe several potential extended sources of gamma-rays, most notably the Galactic Plane for which an upper limit on the gamma-ray flux was set [36].

5.2. Upgrade 2: Pattern selection trigger

In the fall of 1998 a second-level Pattern Selection Trigger (PST) was installed on the Whipple telescope [37], while the wide field-of-view camera was still in regular use. The goal of this upgrade was to lower the telescope’s energy threshold through improved rejection, at the hardware level, of NSB triggers and triggers due to ion-feedback after-pulsing. The PST is essentially a hardware logic device that examines overlapping sectors of pixels in the camera and ascertains if there are adjacent triggering pixels within a sector above the hardware trigger level within a

given time coincidence window. Sectors of 19 pixels were chosen for the Whipple camera since, in a hexagonally symmetrical grid, a hexagonal region of 18 points around a particular point contains both that point’s neighbors and their neighbors. The trigger decision is achieved in hardware, by comparing the discriminator signals within each sector with a pre-programmed delay memory containing mappings for all 2^{19} possible trigger decisions.

The installed system comprised thirteen CAMAC PST modules. The number of required adjacent pixels was adjustable for 2, 3 or 4-fold coincidence. However, since its installation the PST has been operated almost exclusively in 3-fold coincidence, with a coincidence resolving time of ~ 5 ns. In order to provide a jitter-free signal to initiate the ADCs, the previous multiplicity trigger was retained, set at the 2-fold level, and its signal passed through an AND gate with the PST signal, before input to the gate generator, Fig. 4.

To determine the discriminator threshold at which each channel in a camera should operate, a set of rate-versus-threshold curves are typically recorded. Fig. 9 presents

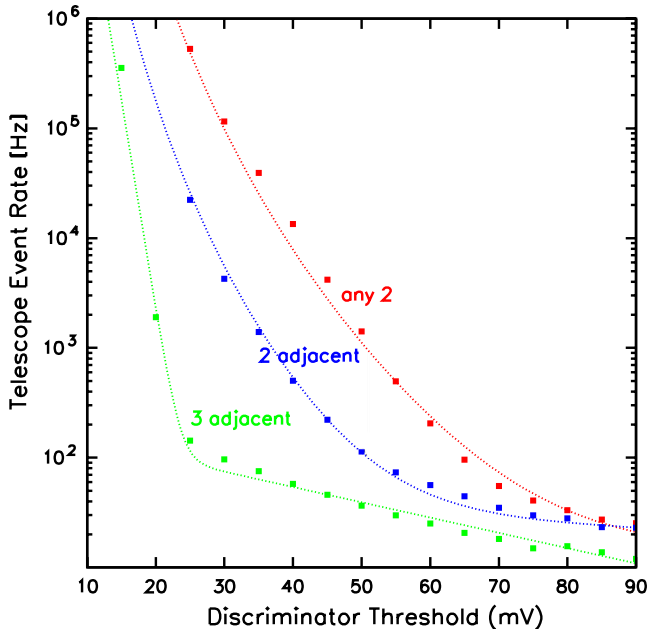


Fig. 9. Whipple 10 m telescope trigger rates as a function of discriminator threshold for two-adjacent and three-adjacent coincidence and simple two-fold multiplicity. Data were obtained using the 331-pixel wide field-of-view camera.

such curves for both the PST, in 2-adjacent and 3-adjacent coincidence, and for the previous simple 2-fold multiplicity trigger. The curves demonstrate that the PST reduces the number of accidental noise triggers by a factor of ~ 10 over the simple 2-fold multiplicity trigger and by a factor of ~ 100 when 3-fold adjacency is required. The reduction in noise triggers provided by the PST enabled the triggering level of the telescope to be set closer to the noise region (the rapidly falling section of the curves in Fig. 9), allowing for an overall reduction in the telescope's energy threshold. After installation of the PST, the discriminator threshold for the wide field-of-view camera was reduced from ~ 75 mV in a 2-fold multiplicity configuration to ~ 60 mV with a 2-adjacent PST condition.

Further evidence for a reduction in the telescope's energy threshold was provided by an increase in the number of triggered events attributable to local cosmic-ray muons. Since muon rings and arcs manifest themselves as long yet faint events at the focal plane compared with the more compact and brighter cosmic-ray images, they populate a region of the LENGTH/SIZE¹ distribution that is distinct from cosmic-ray events (i.e. larger LENGTH/SIZE values). The post-PST LENGTH/SIZE distribution indicated a significant increase in the number of muon events when compared to the pre-PST distribution, as expected

¹ LENGTH is a measure of the signal-weighted r.m.s spread of pixel signals in corrected ADC counts parallel to the major axis of an ellipse fitted to an air-shower image in the camera. SIZE refers to the number of corrected ADC counts in the image and provides a measure of the Cherenkov intensity of an event. For more details see Reynolds et al. [33], Fegan [30,34] or Lessard et al. [35].

for the lower energy threshold provided by the PST. For details see Bradbury and Rose [37].

Indeed, while the PST has provided the Whipple 10 m telescope with a low hardware energy threshold for gamma-ray observations, the high flux of muons at that threshold has effectively limited the usefulness of the low-energy data. Although several attempts at salvaging low-energy events have been undertaken, for example using a Kernel analysis [39], the ultimate solution is a two- (or more) telescope coincidence trigger to eliminate the local muon signal, as demonstrated by the HEGRA [9] and H.E.S.S. [38] experiments. VERITAS [11] will also provide this solution.

5.3. Upgrade 3: High-resolution camera

In the fall of 1999 a small-pixel, high-resolution camera, comprising 490 PMTs, was installed on the Whipple telescope. This camera was the final upgrade of the telescope's focal plane instrumentation and it is currently still in use. The high-resolution camera was composed of 379 inner 13 mm PMTs in a hexagonal arrangement, surrounded by 111 outer 28 mm PMTs in three concentric rings. The total field-of-view subtended by the camera was 3.8° , with each inner pixel observing a 0.12° patch of sky, and each outer pixel 0.26° . A schematic layout of the high-resolution camera is shown in Fig. 3f. Of the inner 379 PMTs, the first 331 were used by the PST for triggering. The objective of the upgrade was to examine the anticipated gain in sensitivity, through superior gamma/hadron separation and lower energy threshold, to be realized by employing such a finely pixelated camera. Only one other camera with similarly fine pixelation has been employed on a IAC telescope to date, that of the CAT telescope [8].

The PMTs of the inner camera were Hamamatsu R647 tubes, while those of the outer camera were Hamamatsu R1398, retained from the previous wide field-of-view camera. The spectral response of a sample inner tube is shown in Fig. 7. PMT rise times were measured to be of the order of 1.0 ns; this is sufficient given the bandwidth of the signal cables and the amplifiers used in the system. The voltages across all PMTs, both inner and outer, were set for equal response under uniform light illumination. Since their installation the PMTs have operated with an average gain of around 1.1×10^6 , which was maintained by occasional HV increases to offset PMT ageing. The trigger threshold of the camera, for most of its lifetime, has been maintained at roughly 30 photoelectrons, spread over 3-adjacent-pixels.

As was the case for the wide field-of-view camera, light-concentrating cones were employed at the focal plane of the high-resolution instrument to reduce the amount of dead space between channels. Lightcones were particularly important given the small size, and hence relatively large percentage of inter-pixel dead space ($\sim 60\%$), of the PMTs used in the inner camera (the PMTs of the outer camera were not equipped with lightcones). The concentrators

deployed were intersecting straight cones machined from a single piece of acrylic, flame polished and aluminized by vacuum evaporation. The lightcones provided for a $\sim 38\%$ increase in the amount of light collected by the inner camera.

5.3.1. Optical fibers

As part of the high-resolution camera upgrade, analog optical fibers (62.5/125 μm graded-index multinode glass fiber, bandwidth of 200 MHz/km) were installed to transmit signals from the outer 111 pixels directly from the camera to the data acquisition electronics [40]. Their installation on the Whipple telescope was an experiment to test their durability and reliability in an observatory setting, while also offering the practical advantage of narrow width in the crowded conduits of a telescope originally designed for a one-pixel camera in 1968.

Despite promising laboratory results, the performance of the optical fiber system at the Whipple Observatory was disappointing overall. In practical terms, the fibers were found to have a wide variation in gain and to require a high degree of protection and delicate handling. Replacement of broken fibers was found to be difficult and time consuming. Although the optical fiber system showed some potential as an alternative to coaxial cable for high bandwidth analog transmission, it was clear that without improvements to both the electronics and to the robustness of the fibers their disadvantages, for use on the Whipple 10 m telescope, outweighed their advantages.

5.3.2. Use of the outer pixels

Several attempts at incorporating the signals from the outer 111 pixels of the high-resolution camera were undertaken, including renormalizations based on simulated data and on the ratio of the physical areas of the two sets of PMTs. However, all efforts to include the outer channels in the data analysis were hindered due to the inherent instability of their signals, resulting from the unsuccessful commissioning of the optical fiber system. The outer PMTs were ultimately removed in 2002 and deployed on a different experiment.

5.3.3. Usefulness of the high-resolution camera

At present the high-resolution camera, without the outer pixels (Fig. 3g), has been successfully operated on the Whipple telescope for about six years. Although the field-of-view of the camera is the smallest of any employed on the telescope, it has, nevertheless, been used to discover, monitor, and study seven sources of VHE gamma-rays with high statistical significance. These sources include the Crab Nebula, Markarian 421, Markarian 501, H1426 + 428 (discovered using the high-resolution camera), 1ES 1959 + 650, 1ES 2344 + 514 and Sgr A*. It has also been used to place upper limits on the VHE gamma-ray flux from a large number of other sources; for example see Fegan et al. [41], Falcone et al. [42], Horan et al. [43], de la calle Pérez et al. [44], Hall et al. [45].

5.4. Upgrade 4: Biased mirror alignment

The Whipple 10 m reflector was designed and built in 1968 for a single-pixel light detector of 1° diameter at the focal plane. The PSF of the original instrument was 0.15° ; adequate for a detector of 1° diameter. When the 490-pixel high-resolution camera was installed in 1999 the PSF of the telescope was initially measured at 0.18° ; considered poor for a camera with a pixel diameter of 0.12° . Deterioration of the PSF can be attributed to the weight of the 490-pixel detector, which exceeds the original design specifications of the telescope by a factor of two. The extra load has the effect of deforming the telescope's OSS as it moves in elevation, thereby increasing the PSF. The extent of the OSS deformation is shown in Fig. 10 for an elevation change from 0° to 90° . Measurements of the OSS deformation were made by clamping small lasers onto individual mirrors and examining the motion of each laser spot at the focal plane as a function of telescope elevation.

During the 2001/2002 observing season a biased alignment of the Whipple telescope's mirrors was undertaken. The purpose of the biased alignment was to optimize the telescope's PSF at typical observing elevations by introducing an intentional mis-alignment at the stow position. Through mis-aligning the mirrors at the stow position by the previously measured degree of their displacements at 65° elevation but in the opposite direction (most observations are performed around 65° elevation), the effect of telescope deformation is suppressed during observations. The success of the biased alignment can be seen in Fig. 11, showing PSF measurements as a function of elevation, taken before and after the procedure was carried out.

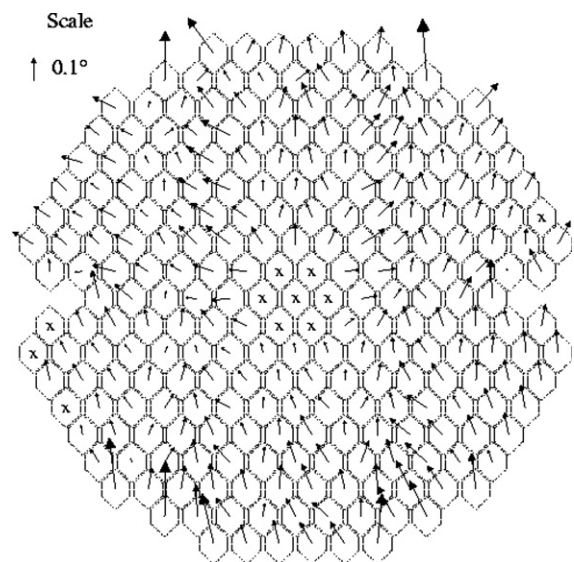


Fig. 10. Angular tilt of the facet-mirrors, due to OSS deformation, as the telescope is moved in elevation from 0° to 90° . X corresponds to no measurement made.

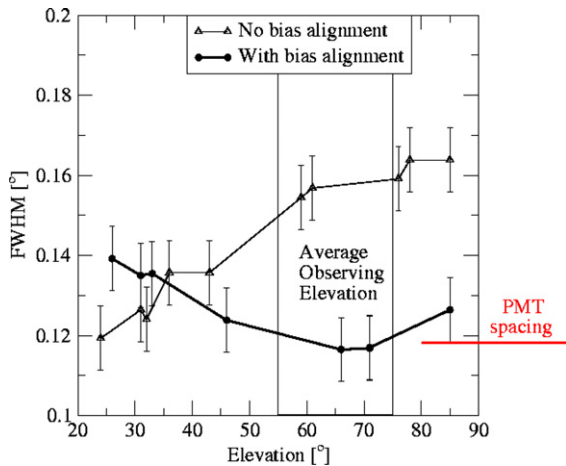


Fig. 11. Measurements of the PSF of the telescope taken over a range of elevations before and after biased alignment. A clear improvement in the PSF in the elevation range of average observing (55–75°) is evident after biased alignment. Shown for reference is the spacing of the PMTs in the high-resolution camera.

6. Summary and conclusion

The GRANITE hardware upgrade of the Whipple 10 m telescope was accomplished in four distinct phases between 1996 and 1999. Two cameras were installed; a wide field-of-view 331-pixel camera and a high-resolution camera. The wide field-of-view instrument was successfully utilized for two years, during which time a Pattern Selection Trigger was installed and tested. The PST allowed for trigger operation at a low discriminator threshold through online suppression of NSB triggers and triggers due to ion-feedback after-pulsing within the PMTs. Use of the PST was continued following installation of the high-resolution camera in 1999, and the PST-enabled 379-pixel camera has been in continuous stable operation on the Whipple telescope since then.

The GRANITE upgrade of the Whipple 10 m telescope, while delivering improved sensitivity for Whipple gamma-ray observations in and of itself, has provided valuable experience and the lessons learned have been incorporated into the design of VERITAS. In particular the VERITAS telescopes incorporate moderately wide field-of-view cameras ($\sim 3.5^\circ$) not unlike the 331-pixel instrument, light-concentrating cones, similar CAMAC-based PSTs utilizing constant fraction discriminators, and a biased mirror alignment procedure to compensate for OSS deformation. As a stereoscopic IAC telescope array, VERITAS will overcome the inhibitive muon background at low energies—that prevented full exploitation of the low-energy threshold provided by the GRANITE PST—enabling observations of low-energy gamma-ray sources such as pulsars, distant AGN and gamma-ray bursts. The stereoscopic IAC technique will also provide other important benefits such as improved angular and energy resolution that are difficult to achieve with a single, independent telescope such as the Whipple 10 m. Indeed, as demonstrated by recent excit-

ing results from the HESS collaboration [46,2,47], there is great potential for discovery using a stereoscopic array of powerful IAC telescopes.

Acknowledgements

This research is supported by grants from the US Department of Energy, the US National Science Foundation, the Smithsonian Institution, by NSERC in Canada, by Science Foundation Ireland and by PPARC in the UK. We also acknowledge the anonymous referee for his meticulous reading of the paper and many useful comments.

References

- [1] T.C. Weekes, Very high energy gamma-ray astronomy, in: Trevor C. Weekes (Ed.), *IoP Series in Astronomy and Astrophysics*, The Institute of Physics Publishing, Bristol, UK, 2003, ISBN 0750306580.
- [2] W. Hofmann, in: *Proceedings of 29th International Cosmic Ray Conference, Pune 2005*, vol. 10, 2006, pp. 97–114.
- [3] J.V. Jelley, N.A. Porter, *Quarterly Journal of the Royal Astronomical Society* 4 (1963) 275.
- [4] J.E. Grindlay, 1971, *SAO Special Report*, No. 334.
- [5] T.C. Weekes, K.E. Turver, *ESA SP-124: Recent Advances in Gamma-Ray Astronomy*, 279, 1977.
- [6] M.F. Cawley et al., *Experimental Astronomy* 1 (1990) 173.
- [7] T.C. Weekes et al., *ApJ* 342 (1989) 379.
- [8] A. Barrau et al., *Nuclear Instruments and Methods in Physics Research A* 416 (1998) 278–292.
- [9] A. Daum et al., *Astroparticle Physics* 8 (1997) 1.
- [10] R.A. Ong, in: *Proceedings of 29th International Cosmic Ray Conference, Pune 2005*, vol. 10, 2006, pp. 329–356.
- [11] T.C. Weekes et al., *Astroparticle Physics* 17 (2002) 221.
- [12] J.A. Hinton, *New Astronomy Reviews* 48 (2004) 331.
- [13] E. Lorenz, *New Astronomy Reviews* 48 (2004) 339.
- [14] R. Enomoto et al., *Astroparticle Physics* 16 (2002) 235.
- [15] G.G. Fazio et al., *Canadian Journal of Physics* 46 (1968) 451.
- [16] J.P. Finley, The VERITAS Collaboration 2001, in: *Proceedings of 27th International Cosmic Ray Conference, Hamburg*, vol. 7, pp. 2827.
- [17] M. Punch et al., *Nature* 358 (1992) 477.
- [18] J.M. Davies, E.S. Cotton, *Journal of Solar Energy* 1 (1957).
- [19] D.A. Lewis, *Experimental Astronomy* 1 (1990) 213–226.
- [20] H.M. Badran, *Nuclear Instruments and Methods in Physics Research A* 524 (2004) 162–168.
- [21] H.J. Rose, in: *Proceedings of 24th International Cosmic Ray Conference, Rome*, vol. 2, 1995, p. 766.
- [22] G. Vacanti et al., *Astroparticle Physics* 2 (1994) 1.
- [23] M. Schroedter, 2004, PhD Thesis, University of Arizona.
- [24] M.P. Kertzman, G.S. Sembroski, *Nuclear Instruments and Methods in Physics Research A* 343 (1994) 629.
- [25] G. Mohanty et al., *Astroparticle Physics* 9 (1998) 15.
- [26] S. Lebohec, C. Duke, <http://www.physics.utah.edu/gammaray/GRISU/>.
- [27] K. Kosack et al., *ApJ* 608 (2004) L97.
- [28] A.D. Kerric et al., *ApJ* 452 (1995) 588.
- [29] M. Catanese et al., *ApJ* 501 (1998) 616.
- [30] D.J. Fegan, *Space Science Reviews* 75 (1996) 137.
- [31] M.F. Cawley, in: *Workshop Towards a Major Cherenkov Detector (Calgary)*, 1993, p. 176.
- [32] Hillas, A.M., Patterson, J.R. 1987, *NATO ASIC Proc. 199: Very High Energy Gamma Ray Astronomy*, 243.
- [33] P.T. Reynolds et al., *ApJ* 404 (1993) 206.
- [34] D.J. Fegan, *Journal of Physics G Nuclear Physics* 23 (1997) 1013.

- [35] R.W. Lessard, J.H. Buckley, V. Connaughton, S. Le Bohec, *Astroparticle Physics* 15 (2001) 1.
- [36] S. LeBohec et al., *ApJ* 539 (2000) 209.
- [37] S.M. Bradbury, H.J. Rose, *Nuclear Instruments and Methods in Physics Research A* 481 (2002) 521–528.
- [38] S. Funk et al., *Astroparticle Physics* 22 (2004) 285.
- [39] S. Dunlea, P. Moriarty, D.J. Fegan, in: *Proceedings of 27th International Cosmic Ray Conference, Hamburg, vol. 7, 2001*, p. 2939.
- [40] I.H. Bond, et al., in: *Proceedings of 27th International Cosmic Ray Conference, Hamburg, vol. 7, 2001*, pp. 2904.
- [41] S.J. Fegan et al., *APJ* 624 (2005) 638.
- [42] A.D. Falcone et al., *ApJ* 613 (2004) 710.
- [43] D. Horan et al., *ApJ* 603 (2004) 51.
- [44] I. de la Calle Pérez et al., *ApJ* 599 (2003) 909.
- [45] T.A. Hall et al., *ApJ* 583 (2003) 853.
- [46] F. Aharonian et al., *Nature* 439 (2006) 695.
- [47] F. Aharonian et al., *Science* 307 (2005) 1938.